

Measurement of the x-ray mass-attenuation coefficients of gold, derived quantities between 14 keV and 21 keV and determination of the bond lengths of gold

This article has been downloaded from IOPscience. Please scroll down to see the full text article.

2010 J. Phys. B: At. Mol. Opt. Phys. 43 085001

(<http://iopscience.iop.org/0953-4075/43/8/085001>)

View [the table of contents for this issue](#), or go to the [journal homepage](#) for more

Download details:

IP Address: 128.250.144.144

The article was downloaded on 02/11/2011 at 03:56

Please note that [terms and conditions apply](#).

# Measurement of the x-ray mass-attenuation coefficients of gold, derived quantities between 14 keV and 21 keV and determination of the bond lengths of gold

J L Glover<sup>1</sup>, C T Chantler<sup>1</sup>, Z Barnea<sup>1</sup>, N A Rae<sup>1</sup> and C Q Tran<sup>2</sup>

<sup>1</sup> School of Physics, University of Melbourne, Victoria 3010, Australia

<sup>2</sup> Department of Physics, La Trobe University, Victoria 3086, Australia

E-mail: [chantler@unimelb.edu.au](mailto:chantler@unimelb.edu.au)

Received 30 December 2009, in final form 11 February 2010

Published 23 March 2010

Online at [stacks.iop.org/JPhysB/43/085001](http://stacks.iop.org/JPhysB/43/085001)

## Abstract

The x-ray mass-attenuation coefficients of gold are measured at 91 energies between 14 keV and 21 keV using synchrotron radiation. The measurements are accurate to between 0.08% and 0.1%. The photoelectric mass-absorption coefficients and the imaginary component of the form factors of gold are also determined. The results include the  $L_I$  edge and are the most accurate and extensive gold dataset available in this energy range. An analysis of the  $L_I$  edge XAFS showed excellent agreement between the measured and simulated XAFS and yielded highly accurate values of the bond lengths of gold. When our results are compared with earlier measurements and with predictions of major theoretical tabulations, significant discrepancies are noted. The comparison raises questions about the nature of discrepancies between experimental and theoretical values of mass-attenuation coefficients.

(Some figures in this article are in colour only in the electronic version)

## 1. Introduction

X-ray form factors and attenuation coefficients describe the interaction of x-rays with matter and are widely applied throughout science. For example, medical x-ray images and CT scans are generated by measuring the spatial variation of the x-ray attenuation by the body [1, 2]. The associated values of the imaginary part of the atomic form factor are used in crystallography for the elucidation of protein structures by the multiple anomalous dispersion (MAD) technique [3, 4]. Attenuation coefficients are also essential for the study of bonding and the local atomic structure of materials and molecules using the x-ray absorption fine structure and near-edge structure analysis [5, 6]. More generally, with the increasing use of x-rays at medical facilities and synchrotrons, it is essential to have accurate reference values of mass-attenuation coefficients and form factors. Despite their wide use, large discrepancies exist in the experimental [7, 8] and theoretical literature [9] and for most elements the value of the

mass-attenuation coefficient is only known to an accuracy of a few per cent.

X-ray mass-attenuation coefficients can be calculated using relativistic quantum mechanics. Although several assumptions are necessary to make them tractable, such calculations have been made and compiled into theoretical tabulations. The two theoretical tabulations recommended by the National Institute of Standards and Technology (NIST) are XCOM [10] and FFAST [9, 11]. These tabulations can be critically tested by comparison with high-accuracy experiments, and in recent years there have been several notable comparisons—mostly for medium-Z elements and often at K-edge energies. Significant discrepancies were observed between the tabulations and experiment, especially at and above the K-edge where differences reached 5% [12–15]. In contrast, there are very few high-quality experimental measurements available for high-Z elements or at L edges and in these regions the accuracy of theory is yet to be critically tested.

**Table 1.** A summary of previous measurements of the mass-attenuation coefficient of gold between 14 keV and 22 keV. Only measurements providing estimates of experimental uncertainties are listed. The list was compiled from J H Hubbell’s comprehensive bibliography of attenuation coefficient measurements [19]. Available data for gold in this energy range are sparse—the total number of measurements is only 25. All the measurements claim an experimental uncertainty greater than 1% except for one measurement by Alonso and Grodzins and three by Hughes *et al*.

Author(s) [Ref]	X-ray source	Energy		Reported accuracy (%)
		Range (keV)	No	
Allen [20]	X-ray tube	12.4–17.5	4	1
Laubert [21]	X-ray tube	14.1–20.2	8	3
Alonso and Grodzins [18]	Nuclear Zeeman effect	14.4	1	0.1
Bearden [22]	X-ray tube	15–20	2	1
Hughes <i>et al</i> [17]	Electron microprobe	14–22	3	0.5
Parthasaradhi and Hansen [23]	Radioactive isotope	14–21	2	2
Hanser and Sellers [24]	Radioactive isotope	6–15	1	1.9
Rao and Shahnawaz [25]	Radioactive isotope	14.4	1	2
Del Grande [26]	X-ray tube	15–20	3	3

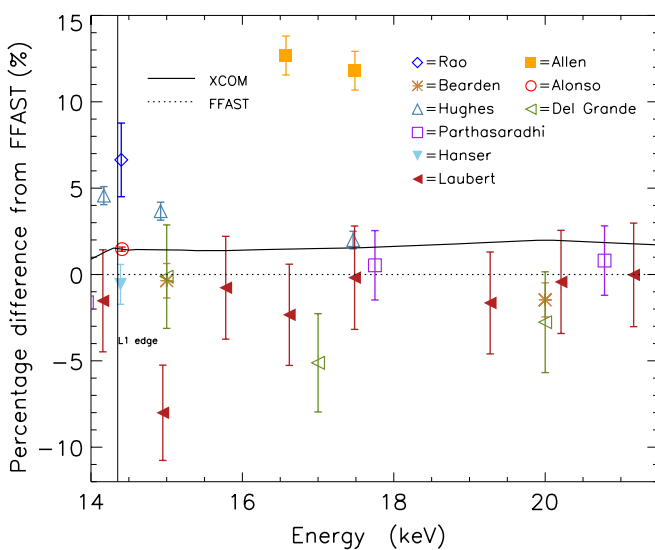


**Figure 1.** A comparison of past measurements of the mass attenuation coefficient of gold between 14 keV and 22 keV following table 1. The experimental measurements are plotted as a percentage difference ( $100 \frac{\text{EXP} - \text{FFAST}}{\text{FFAST}}$ ) from the FFAST theoretical tabulation of mass-attenuation coefficients [9, 11]. The FFAST tabulation is plotted as a dotted line and the XCOM tabulation [10] is plotted as a solid line. The energy of the gold  $L_1$  edge is indicated by the solid vertical line—more measurements are needed in this region where the mass-attenuation coefficient changes rapidly. The measurements disagree by up to 10% at some energies and the two most accurate measurements (Hughes *et al* and Alonso and Grodzins) appear to disagree near the gold  $L_1$  edge. The legend refers to each dataset by the name of the first author (see table 1).

There are a few previous measurements of the mass-attenuation coefficient of gold in this energy range. The measurements typically reported experimental uncertainties in the 0.5–3% range, although some are published without estimates of their uncertainties. Table 1 summarizes the previous measurements which included uncertainty estimates (a total of 25 measurements from eight experiments). These measurements are plotted in figure 1. A higher energy x-ray extended range technique (XERT) measurement of gold was recently completed between 38 keV and 50 keV [16].

The previous measurements disagree with one another by up to 15% and 10 standard deviations. The work of Allen is particularly discrepant from the other data, and is more than 10% higher than the other measurements, although this is a very early measurement. The most accurate experiments were performed by Hughes *et al* [17] and Alonso *et al* [18]. In the region of the  $L_1$  edge, these two experiments appear discrepant and there are reasons to doubt the uncertainty estimates of Alonso *et al* (see section 8 of this paper).

The discrepant and unreliable nature of many mass-attenuation coefficient measurements was recognized long ago and has been discussed in detail elsewhere [7]. A notable response to the issue was the *X-ray Attenuation Project*, which was initiated by the International Union of Crystallography (IUCr) [7, 27]. The project aimed to ‘identify those experimental techniques which are likely to minimize systematic error’. The project was a major development, but reliable measurements of mass-attenuation coefficients are still not available for most elements.

In this paper we present measurements of the x-ray mass-attenuation coefficient of gold at 91 energies between 14 keV and 21 keV. The results are accurate to between 0.08% and 0.1%. The photoelectric mass-absorption coefficient and imaginary part of the form factor of gold were also determined from the mass-attenuation coefficient after subtraction of the scattering contribution. Several sources of systematic error were recognized and corrected and this led to an improvement in the overall accuracy of the results. These are the most accurate currently available measurements of the mass-attenuation coefficient of gold in this energy range and the first high-accuracy measurement of an L edge. Our results include the gold  $L_1$  edge and its associated fine structure and should prove useful as an XAFS standard spectrum. We perform an XAFS analysis on the data and determine accurate values of the bond lengths of gold.

## 2. Experimental details

### 2.1. Experimental technique

Our experiment utilized the x-ray extended range technique (XERT) [8, 14] to measure the mass-attenuation coefficient of

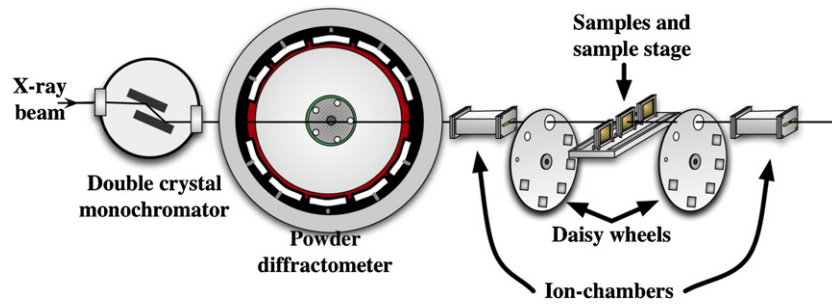


**Figure 2.** A schematic of the experimental setup used during this XERT experiment (not to scale). The x-ray beam energy was measured (after monochromation) using a powder diffractometer. Ion chambers were used to measure the intensity of the x-ray beam upstream and downstream of the gold foil samples.

gold to high accuracy. The measurements were made at the Australian National Beamline Facility (ANBF) at the bending-magnet beamline 20B of the Photon Factory synchrotron in Tsukuba, Japan. The accuracy and extent of our results would not have been possible without the high flux and tuneable energy of synchrotron x-rays.

The XERT is used for measuring mass-attenuation coefficients, form factors and the x-ray absorption fine structure (XAFS) and has produced the most accurate absolute measurements in the literature [28]. In order to achieve such an accuracy, the XERT detects and corrects a number of systematic errors including harmonics [29]; finite-spectral bandwidth [30]; scattering and fluorescence [31]; sample roughness [32]; and attenuation by the detectors and air path.

In the XERT, the magnitude of any systematic errors is measured by analysing how they affect the measurements, and how these effects change as experimental parameters are varied. Indeed, measurements are carried out over an extended range of experimental parameter space in order to discover and characterize systematic errors. In this experiment, we corrected for the effects of several systematic errors including fluorescence, sample roughness and energy drift (see section 5).

A schematic of the experimental setup is shown in figure 2. The x-ray beam was monochromated using a detuned double-reflection monochromator utilizing a monolithic silicon 111 crystal. The beam then passed into a powder diffractometer so that the energy of the x-rays could be accurately measured. A pair of 186 mm long ionization chambers were placed upstream and downstream of the gold samples and run in serial-flow mode using nitrogen gas. Daisy wheels were also placed upstream and downstream of the samples to provide control of the angular acceptance of the detectors using three apertures that subtended solid angles of 1.05, 4.07 and 25.4 msr (milliradian). Fifteen aluminium foils were mounted around the circumference of the daisy wheels (with thicknesses varying over several orders of magnitude) to provide additional information about thickness-dependent systematic errors. The sample stage held three gold foils and was configured so that it could translate along and rotate about the horizontal and vertical axes perpendicular to the beam. This allowed for automated control of the position of the foil samples in the x-ray beam to an accuracy of 1  $\mu\text{m}$  [33].

**Table 2.** The nominal thicknesses of the gold foils. Some foils were replaced at 20 keV, 19 keV and 18 keV. Bold numerals mark the foils which were subjected to the full-foil mapping (see section 4).

Energy range (keV)	Foil in position 1	Foil in position 2	Foil in position 3
21–20	<b>25</b> $\mu\text{m}$ (a)	<b>25</b> $\mu\text{m}$ (b)	15 $\mu\text{m}$
20–19	<b>25</b> $\mu\text{m}$ (a)	9 $\mu\text{m}$	15 $\mu\text{m}$
19–18	5 $\mu\text{m}$	<b>25</b> $\mu\text{m}$ (b)	15 $\mu\text{m}$
18–14.3	5 $\mu\text{m}$	9 $\mu\text{m}$	15 $\mu\text{m}$

## 2.2. The gold foils

The five gold foils that were used in the experiment were supplied by Goodfellow and ranged in thickness from 5  $\mu\text{m}$  to 25  $\mu\text{m}$ . Each foil was securely mounted in a bevelled Perspex holder to ensure mechanical stability for the entire experiment. Table 2 lists the foils measured in each energy range. The foils are referred to by their nominal thicknesses, but this is purely a label—the nominal thicknesses were not used to calculate anything.

The manufacturer quoted purities were 99.99+% for the two 25  $\mu\text{m}$  reference foils and 99.9% for the other foils. The effect of impurities on the measured mass-attenuation coefficients is discussed in subsection 5.5.

The mass of each foil was determined by repeated weighing on a microgram scale (resolution 1  $\mu\text{g}$ ) to an accuracy of between 0.003% and 0.015%. The areas of the samples (nominally 25 mm by 25 mm) were measured using a Mitutoyo PJ300 optical comparator (resolution  $5 \times 5 \mu\text{m}^2$ ) to an accuracy of between 0.04% and 0.05%.

The integrated column density, averaged over the entire foil, was calculated from the mass  $m$  and area  $A$  using the equation

$$[\rho t]_{\text{ave}} = \frac{m}{A}. \quad (1)$$

The integrated column density  $[\rho t]$  is to the density  $\rho$  multiplied by the thickness  $t$  for an ideal sample of uniform density and thickness.

For foil 25  $\mu\text{m}$  (a), the average integrated column density was  $0.049756 \pm 0.000026 \text{ g cm}^{-2}$ . For foil 25  $\mu\text{m}$  (b), the average integrated column density was  $0.049915 \pm 0.000024 \text{ g cm}^{-2}$ . These values are used in section 4 to determine the absolute mass-attenuation coefficient.

### 3. The attenuation of the gold foils

The Beer–Lambert equation describes the attenuation of an x-ray beam

$$\left[\frac{\mu}{\rho}\right][\rho t] = -\log\left(\frac{I}{I_0}\right), \quad (2)$$

where  $I_0$  and  $I$  are the x-ray beam intensities incident and transmitted through the foil. Here, the mass-attenuation coefficient  $\left[\frac{\mu}{\rho}\right]$  is equal to the linear-attenuation coefficient  $\mu$  divided by the density  $\rho$  for an ideal sample of uniform density.

In practice, the quantity on the left-hand side of equation (2) represents the attenuation of all the matter between the front of the upstream ion chamber and the front of the downstream ion chamber. To determine the attenuation of the foil alone, two measurements were made: one with the foil in the x-ray beam and one with the foil removed. The attenuation of the gold foil was then calculated using [14, 28]

$$\left[\frac{\mu}{\rho}\right][\rho t]_G = \left[\frac{\mu}{\rho}\right][\rho t]_{G+IC1+A} - \left[\frac{\mu}{\rho}\right][\rho t]_{IC1+A}, \quad (3)$$

where the subscripts  $A$ ,  $G$  and  $IC1$  refer to the airpath, gold foil and upstream ion chamber (including window materials) respectively. When the incident and transmitted intensities are measured simultaneously, fluctuations in the intensity of the x-ray beam should not affect the measured attenuation. This method also allows normalization for any differences in efficiency and electronic gain between the two ion chambers [34]. Dark current subtraction and uncertainty determination is discussed elsewhere [28].

The attenuation of the foils was measured at 91 energies between 14 keV and 21 keV for at least three foils per energy. This energy range included the gold  $L_I$  edge at 14.35 keV and the associated fine structure (XAFS) just above it. In order to properly characterize this fine structure and the edge, measurements in this region were made with a finer energy separation.

The measured attenuations of foils are plotted against energy in figure 3. The sample changes were coordinated so that, where possible, the relative attenuation satisfied an extended Nordfors criterion ( $0.5 \leq \left[\frac{\mu}{\rho}\right][\rho t] \leq 5$ ) so that optimal statistical accuracy was maintained [14, 35].

#### 3.1. Determining the photon energies

The mass-attenuation coefficient must be measured at well-defined energies, since it is an energy-dependent quantity. We determined the energy using a powder diffractometer and two powder standards with well-known lattice parameters and diffraction properties. We chose the NIST powder-diffraction standards (Si 640b [36] and LaB<sub>6</sub> 660 [37]) which were the most accurate available. The methodology and final results of the powder diffraction measurements taken during this experiment are described in [38].

Each mass-attenuation coefficient measurement had a nominal x-ray energy reading from the motor controlling the angular movement of the monochromator crystals. These nominal encoder energies generally have offset and scaling

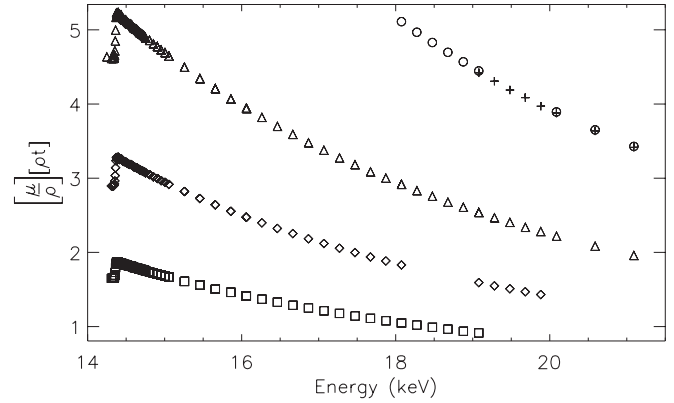


**Figure 3.** Measured values of the relative mass-attenuation coefficient are plotted against energy. Each symbol is associated with a particular foil:  $\square$  5  $\mu\text{m}$ ;  $\diamond$  9  $\mu\text{m}$ ;  $\triangle$  15  $\mu\text{m}$ ; + 25  $\mu\text{m}$  (a);  $\circ$  25  $\mu\text{m}$  (b).

errors and do not constitute an accurate measurement of x-ray energies [38].

A linear model was used to map the nominal energies onto the calibrated energies following [33]. The energy of the x-ray beam used for each measurement was thereby determined to an accuracy of between 0.3 eV and 1.3 eV. A full list of the x-ray energies and their associated uncertainties is given along with the main results in section 6.

### 4. Absolute determination of the mass-attenuation coefficient of gold

The absolute value of the mass-attenuation coefficient was determined using the full-foil mapping technique which can be summarized as follows. The mass of the foil was divided by its area in order to determine the average mass per unit area  $[\rho t]_{\text{ave}}$  (see subsection 2.2). The average attenuation  $\left[\frac{\mu}{\rho}\right][\rho t]_{\text{ave}}$  was determined by measuring the attenuation across the area of the foil by means of an x-ray raster scan. Finally, the average attenuation was divided by the average mass per unit area to determine the absolute mass-attenuation coefficient in units of  $\text{cm}^2 \text{g}^{-1}$ .

#### 4.1. Removing the attenuation of the sample holder

A Perspex sample holder was used to mount the thin foils securely in place, but it also attenuated the x-ray beam. The effect of the attenuation of the holder had to be removed from the raster scan, so that the average attenuation of the foil could be calculated. The attenuation of the foil and holder is plotted in figure 4. A model of the attenuation of foil and holder was constructed and fitted to the data [39]. The absence of any significant, circular-shaped artefacts in the residuals indicates that the shape of the holder was properly modelled and that the holder removal procedure was successful. Once the attenuation of the holder was well characterized it was subtracted from the data, leaving an attenuation map of the foil alone.

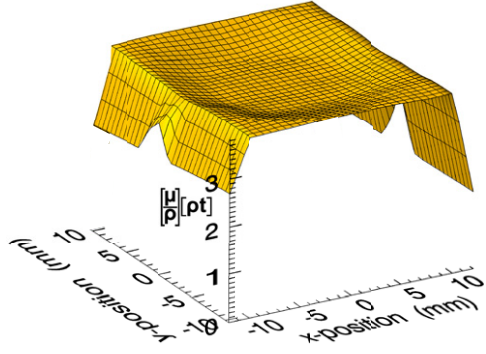


**Figure 4.** The attenuation of gold foil 25  $\mu\text{m}$  (a) and its holder are shown. One can clearly see the effect of the circularly bevelled holder. See also figure 5.

#### 4.2. Determining $[\frac{\mu}{\rho}][\rho t]_{\text{ave}}$ and its uncertainty

**4.2.1. Modelling the foils.** The foil was modelled as a square with two parameters  $(x_0, y_0)$  defining the position of its centre and one describing the axis of the foil. This model was fitted to the experimental data from the full-foil mapping. The orientation and foil-centre in the  $x$ -direction were easily fitted with low uncertainty, but the raster scan did not reach the top or bottom of the foil (see figure 5(a)) so the centre in the  $y$ -direction was less accurately defined (1.4 mm uncertainty).

The foil was assumed to have the thickness profile of a truncated wedge and was described by the formula

$$\left[\frac{\mu}{\rho}\right][\rho t]_{\text{model}} = \left[\frac{\mu}{\rho}\right][\rho t]_0 + m_x(x - x_0) + m_y(y - y_0), \quad (4)$$

where  $[\frac{\mu}{\rho}][\rho t]_0$  is the value of the attenuation at the centre of the foil  $(x_0, y_0)$ . The parameters  $m_x$  and  $m_y$  describe the gradients of the wedge in the  $x$ - and  $y$ -directions respectively. The wedge-profile model was irrelevant for determining the centre and orientation, but was useful for estimating the attenuation beyond the coverage of the raster scan. The model will be denoted by  $F(\vec{x}_j; \vec{P})$ , where  $\vec{x}_j$  is the location of the centre of the  $x$ -ray beam and  $\vec{P}$  is an array of model parameters.

**4.2.2. Determining  $[\frac{\mu}{\rho}][\rho t]_{\text{ave}}$  and its uncertainty.** The purpose of mapping the full foil is to accurately determine the average attenuation  $[\frac{\mu}{\rho}][\rho t]_{\text{ave}}$ :

$$\left[\frac{\mu}{\rho}\right][\rho t]_{\text{ave}} = \frac{1}{A} \sum_i a_i \left[\frac{\mu}{\rho}\right][\rho t]_i, \quad (5)$$

where  $[\frac{\mu}{\rho}][\rho t]_i$  is the  $i$ th measurement of the attenuation made over a region of area  $a_i$ . This summation must be performed over a set of regions that form a complete partition of the foil (therefore  $\sum a_i = A$ ).

For the upper and lower edge regions, where information was limited, the attenuation of the foil was taken from the model  $F(\vec{x}_j; \vec{P})$ . Hence,

$$\left[\frac{\mu}{\rho}\right][\rho t]_{\text{ave}} = \frac{1}{A} \left( \sum_i a_i \left[\frac{\mu}{\rho}\right][\rho t]_i + \sum_j a_j F(\vec{x}_j; \vec{P}) \right). \quad (6)$$

The average attenuation was affected by two types of uncertainties: the uncertainty in the experimental measurements and the uncertainty and covariance of the foil-model parameters. The formula for the uncertainty in the

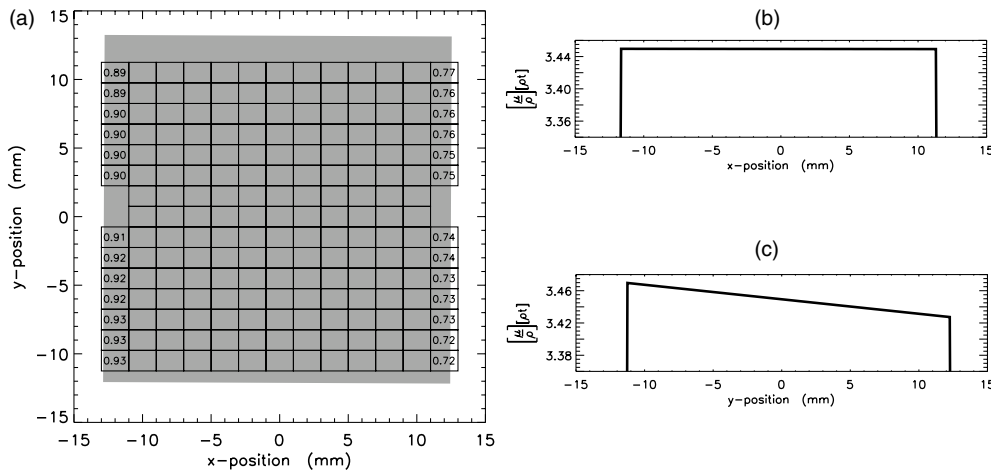


**Figure 5.** The model of the gold foil 25  $\mu\text{m}$  (b) is shown. Part (a) shows the area of the foil over which the full-foil mapping was performed. The large grey square indicates the location and size of the foil. The grid of smaller rectangles shows the footprint of the  $x$ -ray beam during the full-foil mapping. Each rectangle shows the position, size and orientation of the  $x$ -ray beam for one measurement of the full-foil mapping. For some measurements, the  $x$ -ray beam only partially intersected the foil—where that is the case the fraction of the beam that intersected the sample is printed within the appropriate rectangle. The  $x$ -ray beam only intersected the foil at the left and right edges, so we have less information about the position of its top and bottom edges. Diagrams (b) and (c) show the model of the attenuation of the foil. Diagram (b) plots the attenuation of the model of the foil along the line  $y = 0$ . Diagram (c) plots the attenuation of the model of the foil along the line  $x = 0$ .

average attenuation is

$$\sigma_{\left[\frac{\mu}{\rho}\right]_{\text{ave}}}^2 = \sum_i \sigma_{\left[\frac{\mu}{\rho}\right]_{\text{ave},i}}^2 \left(\frac{a_i}{A}\right)^2 \quad (7)$$

$$+ \sum_{jk} \text{COV}(j, k) \left(\frac{\partial^2 \left[\frac{\mu}{\rho}\right]_{\text{ave}}}{\partial P_j \partial P_k}\right)^2, \quad (8)$$

where  $P_j$  is the  $j$ th element of the array of model parameters  $\vec{P}$ .  $\text{COV}(j, k)$  is the covariance between  $P_j$  and  $P_k$ .  $\frac{\partial^2 \left[\frac{\mu}{\rho}\right]_{\text{ave}}}{\partial P_j \partial P_k}$  is the second-order, mixed partial derivative of the average attenuation of the foil with respect to  $P_j$  and  $P_k$ . The first summation gives the uncertainty contribution from the experimental measurements and the second summation gives the contribution from the uncertainty and covariance of the model parameters.

The average attenuation of foil 25  $\mu\text{m}$  (b) was determined using equations (6) and (8):

$$\left[\frac{\mu}{\rho}\right]_{\text{ave}} = 3.4466 \pm 0.0026(0.075\%). \quad (9)$$

For foil 25  $\mu\text{m}$  (a)

$$\left[\frac{\mu}{\rho}\right]_{\text{ave}} = 3.4259 \pm 0.0075(0.22\%). \quad (10)$$

The limiting uncertainty for both foils was due to the uncertainty in  $y_0$ , the  $y$ -component of the centre of the foil. Although this uncertainty was the same for both foils, it caused a larger error in foil 25  $\mu\text{m}$  (a) because of the larger value of  $m_y$  (a vertical shift of  $\Delta y$  causes an error that is proportional to  $m_y \Delta y$ ).

#### 4.3. Perpendicular alignment of the foils

The gold foils were not aligned perfectly perpendicular to the x-ray beam, and the effect of this misalignment had to be corrected for. The angle of the foil with respect to the beam was determined by a rotation scan [39]. The foil was rotated about the  $x$  and  $y$  axes and reached its minimum attenuation when perpendicular to the x-ray beam. Foil 25  $\mu\text{m}$  (a) was misaligned by  $2.14^\circ$  and foil 25  $\mu\text{m}$  (b) by  $2.08^\circ$ . The appropriate correction was applied to the value and uncertainty of the average attenuation [39].

#### 4.4. Absolute determination of the mass-attenuation coefficient of gold at 21 keV

The absolute mass-attenuation coefficient of gold was calculated using

$$\left[\frac{\mu}{\rho}\right] = \frac{\left[\frac{\mu}{\rho}\right]_{\text{ave}}}{\left[\rho t\right]_{\text{ave}}}. \quad (11)$$

The two independent measurements of the mass-attenuation coefficient of gold were  $68.854 \pm 0.15 \text{ cm}^2 \text{ g}^{-1}$  and  $69.048 \pm 0.062 \text{ cm}^2 \text{ g}^{-1}$ . These are in good agreement and were combined to yield the weighted mean of the mass-attenuation coefficient of gold at  $21091.9 \pm 0.6 \text{ eV}$ , which was largely determined by the more accurate of the two

measurements

$$\left[\frac{\mu}{\rho}\right] = 69.021 \pm 0.057 \text{ cm}^2 \text{ g}^{-1}, \quad (12)$$

and was accurate to 0.083%.

#### 4.5. Determining $[\rho t]$ of the other foils

The full-foil mapping procedure was performed on the two thickest samples. We also needed to convert the relative attenuation data from the other foils onto the absolute scale ( $\text{cm}^2 \text{ g}^{-1}$ ). This was done by requiring self-consistency among the measurements at each energy. The integrated-column densities of the foils and their associated uncertainties were determined using a least-squares fitting routine. This minimized the  $\chi^2$  deviation between the mass-attenuation coefficient measurements obtained from the different foils, subject to the constraint that they be consistent with the results of the full-foil mapping.

### 5. Correcting for systematic errors

All attenuation measurements are affected by systematic errors. We were able to identify and accurately quantify a number of these systematics because measurements were taken over an extended range of parameter space. For example, the thickness dependence of a systematic error was detected because measurements were made on a number of foils of different thicknesses. Once a systematic error is accurately modelled, its effect can be removed from the data. We corrected for the effects of x-ray fluorescence, roughness, impurities and monochromator energy drift.

#### 5.1. Harmonics

We determined the harmonic content of the synchrotron beam by measuring the attenuation of 15 aluminium foils with thicknesses that ranged from 10 to 4000  $\mu\text{m}$ . This method of determining the harmonic content using attenuation measurements has been applied to x-rays produced by tube sources [40] and synchrotron radiation [29]. We developed the method, and applied it to measure the harmonic content of the beam at every energy. The measured harmonic content did not differ significantly from zero for any of these measurements. The effective harmonic parameter  $\alpha$  (defined in [41]) remained below  $10^{-5}$  for all our measurements. This demonstrated the linearity of our detection system far beyond the range of our main measurements.

This method has been used successfully at beamline 20B of the Photon Factory to determine the level of harmonic content in the beam [29, 33]. No previous study has detected harmonics above 8 keV at this beamline (after detuning optimization) so our results are consistent with these earlier measurements.

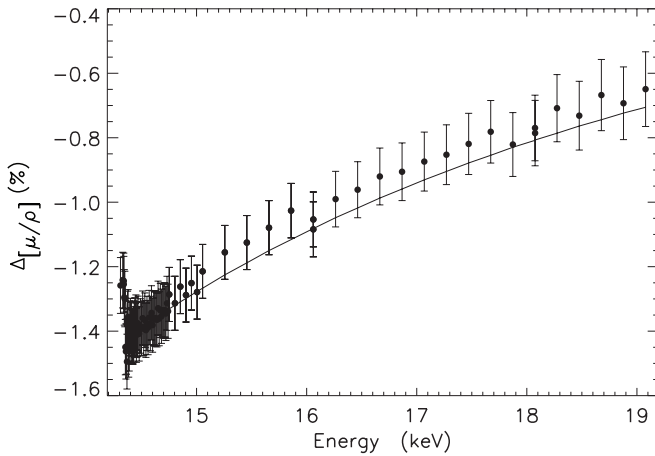


**Figure 6.** This plot shows the percentage discrepancy between the measured mass-attenuation coefficient of the 5 μm foil and the weighted mean of the other foils. A model of the effect of roughness on the measured mass-attenuation coefficient was fitted to the data and the result is plotted as a solid line. Using the model, the roughness of the foil was determined to be 661.7 ± 6.7 nm.

### 5.2. Foil roughness

Foil roughness causes a systematic error in measurements of the mass-attenuation coefficient particularly for thinner foils. For our purposes, roughness is any surface structure or internal inhomogeneity (such as voids in the material) that leads to variation in the amount of material that absorbs the x-ray beam. In this experiment, roughness caused measurements made upon the 5 μm foil to be systematically lower by up to 1.5% [32]. We developed a model that describes the effect of roughness on the measured mass-attenuation coefficient. This model also allowed us to determine the magnitude of roughness of the foil and was the key step in developing a new x-ray-based, roughness-characterization technique used to determine the roughness at sub-micron and nano-levels to accuracies better than 20 nm [32]. The theoretical basis for how roughness affects measurements of the mass-attenuation coefficient is described in [32] along with details of the methodology used to determine the magnitude of the roughness in the 5 μm sample used in this experiment.

There was a clear and systematic discrepancy between the mass-attenuation coefficient measurements made on the 5 μm foil and those made on the thicker, smoother foils. The discrepancy was seen across the entire energy range and is plotted in figure 6. It is caused by roughness and has a smooth dependence on the mass-attenuation coefficient. Since the mass-attenuation coefficient changes with energy, the effect of roughness on our measurements is energy dependent. The form of the discrepancy was predicted using the model, which had one parameter: the magnitude of the roughness  $\sigma_{[\rho t]}$ . The magnitude of the roughness of the 5 μm foil was determined to be

$$\sigma_{[\rho t]_{5\mu\text{m}}} = 0.001\,277\text{ g cm}^{-2} \pm 1.01\%, \quad (13)$$

within the footprint of the x-ray beam. Given a density of 19.3 g cm<sup>-3</sup> for gold, this corresponds to a roughness of

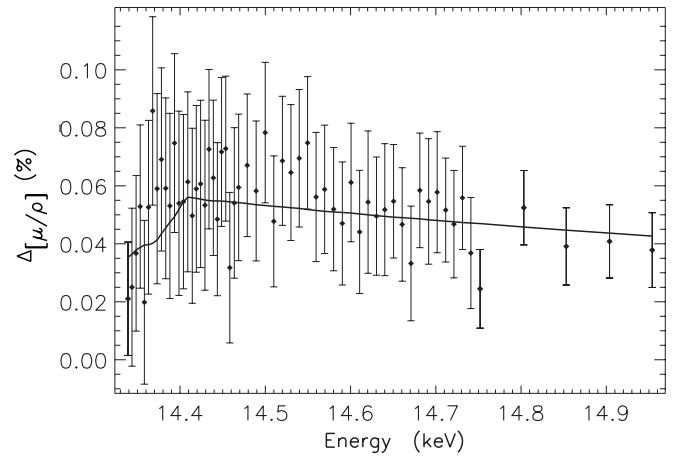


**Figure 7.** The discrepancy between measurements made with the large and medium apertures for the 15 μm foil. The difference between the two measurements is significantly greater than zero. The effect is largest just above the gold L<sub>I</sub> edge. The error bars do not include the uncertainty contribution from the integrated column-density since we are comparing two measurements from the same foil. A model of the effect of fluorescence was fitted to the data and the result is plotted as a solid line. The model and the data are in excellent agreement.

$\sigma_{[t]} = 661.7\text{ nm} \pm 6.7\text{ nm}$ . The best-fit model of the discrepancy due to roughness was compared with experiment and the agreement between the two was excellent. The model prediction is plotted as a solid line in figure 6.

Once the roughness of the foil was accurately characterized, its effect upon the mass-attenuation coefficient was corrected for. This improved the overall agreement between the foils. The uncertainty contribution due to roughness was small (between 0.02% and 0.06%) and only contributed to the 5 μm foil.

### 5.3. Fluorescence

X-ray fluorescence can cause a systematic error in the measured mass-attenuation coefficient [31]. Such a systematic error was observed in our data and was most pronounced at energies just above the gold L<sub>I</sub> edge. The fluorescence was mostly emitted as L $\alpha$  and L $\beta$  radiation [42] and some of it entered our detectors and caused a systematic error.

The effect of fluorescence on our measurements was small, having its largest effect (up to 0.1%) for measurements on the thickest sample just above the L<sub>I</sub> edge. Its effect was most notable when comparing measurements made using different apertures for a given foil. By varying the aperture size, we controlled the number of fluorescent photons entering the detector and could therefore gauge the magnitude of the effect. The difference in the values of the mass-attenuation coefficient obtained using the large and medium apertures is plotted in figure 7—these data are for the 15 μm sample (the thickest foil used at these energies).

We modelled the effect of fluorescence on our measurements in a similar manner to [31] and [28], but took account of some additional effects. The simulation took account of the differing attenuation of the main beam and of

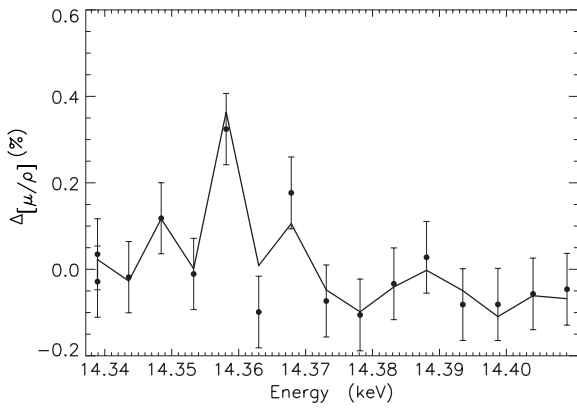


**Figure 8.** The difference between the value of the mass-attenuation coefficient measured on foil 25  $\mu\text{m}$  (b) and the weighted mean of all the foils. The prediction of our model of energy drift is plotted as a solid line. The plot includes the region of the  $L_I$  edge, where the gradient of the mass-attenuation coefficient is large.

fluorescent x-rays by the gold foils, air and ion chambers. We also modelled the different detector efficiencies when detecting the fluorescence and the main x-ray beam. The model was fitted to the data and the agreement between the two was excellent (see figure 7). Finally, the effect of fluorescence was subtracted from our measurements and the resultant contribution to the uncertainty was less than 0.01%.

#### 5.4. Energy drift

The energy of the x-ray beam drifted slightly during the course of some of our measurements. This type of monochromator instability has been observed before at this beamline, during a previous copper experiment [33]. The effects are smaller in these data but they were modelled and removed in the same manner. In both experiments, the monochromator was equipped with a Heidenhain encoder that should have dynamically measured the monochromator angle (and hence the energy) as it drifted. However, as the energy drifted, the encoder reading stayed almost constant while the measured attenuation drifted.

Our measurements were most affected by the energy drift in two situations: after large changes in the monochromator angle; and when the gradient of the mass-attenuation coefficient  $\frac{d[\frac{\mu}{\rho}]}{dE}$  was large. The systematic error in the data was clearest and reached a value of more than 0.45% at the edge (see figure 8). Given sufficient time after each energy change, the monochromator settled towards a stable value in a consistent way.

We modelled the energy drift in a similar manner to that reported in [33]. In our model, the magnitude of the energy drift  $E_{\text{drift}}$  depended on the size of the last energy change  $E_{\text{jump}}$  and the time since the last energy change  $\Delta t$  and was described by the equation

$$E_{\text{drift}} = \alpha (E_{\text{jump}})^\gamma \exp\left(\frac{-\Delta t}{\beta}\right), \quad (14)$$

where  $\alpha$ ,  $\beta$  and  $\gamma$  were fitted parameters.

The energy drift caused a change in the measured mass-attenuation coefficient  $\Delta[\frac{\mu}{\rho}]$  described by

$$\Delta[\frac{\mu}{\rho}] = E_{\text{drift}} \frac{d[\frac{\mu}{\rho}]}{dE}. \quad (15)$$

Equations (14) and (15) describe our model of the energy drift. Figure 8 plots the predicted and observed discrepancy seen in the experiment due to the energy drift and the agreement between the two is excellent. The time constant  $\beta$  was found to be 116 s which is much less than that was seen in [33]. The model was used to correct for the effect of energy drift on our measurements and the appropriate uncertainty contributions were included. At the  $L_I$  edge, energy drift contributed an uncertainty of 0.5% to particular measurements but most were far less affected.

#### 5.5. Impurities

Metallic foils always contain some impurities. The gold foils used in this experiment were provided by Goodfellow and came with estimates of their impurity levels. The manufacturer estimate of the purity of the 25  $\mu\text{m}$  foils was greater than 99.99%. The other foils had a manufacturer-estimated purity of 99.9%. The typical assay of impurities listed by the manufacturer of the 99.9% pure foils was 500 ppm Cu, 300 ppm Ag, 100 ppm Ni, 15 ppm Pb and 15 ppm K. The effect of this level of impurities was calculated and added in quadrature to the final estimate of the uncertainty in the mass-attenuation coefficient. The contribution to the uncertainty was less than 0.06% for the 99.9% pure foils. For the high-purity 25  $\mu\text{m}$  foils the effect of impurities was insignificant.

#### 5.6. Other sources of systematic error

We removed the major sources of systematic error affecting our measurements. This claim can be assessed by checking the consistency of the mass-attenuation coefficient measurements made on the various apertures and foils. Figure 9 shows the size of the discrepancies for every foil and aperture as a function of energy. The great majority of measurements lie within 1 standard deviation of the mean and there is no notable dependence on the thickness or aperture size. The consistency of the measurements suggests that any systematic errors remaining in the data were small.

## 6. Tabulation of results

Table 3 presents measurements of the mass-attenuation coefficient of gold at 91 energies between 14 keV and 21 keV. Values of the photoelectric mass-absorption coefficients and imaginary component of the form factor  $f''$  of gold are also tabulated at the same energies. At each energy, measurements were made using multiple foils and apertures and the final result was determined by taking a weighted mean of all the measurements at that energy. The mass-attenuation coefficient between 14.2 keV and 15 keV (the region of the  $L_I$  edge) is plotted in figure 10.

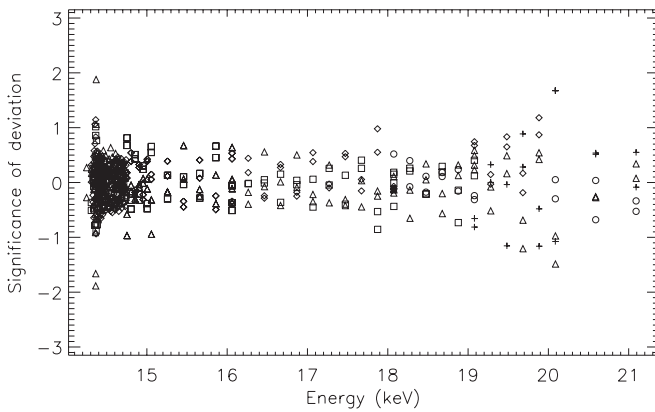


**Figure 9.** This plot shows the level of the deviation of the residuals amongst the measurements from the different samples and apertures. The quantity plotted on the y axis is defined by the formula  $\frac{[\frac{\mu}{\rho}] - [\frac{\mu}{\rho}]}{\sigma_{[\frac{\mu}{\rho}]}}$ . It represents how many standard deviations each measurement is away from the mean. Each symbol in the plot is associated with a particular foil of a given nominal thickness:  $\square$  5  $\mu\text{m}$ ;  $\diamond$  9  $\mu\text{m}$ ;  $\triangle$  15  $\mu\text{m}$ ; + 25  $\mu\text{m}$  (a);  $\circ$  25  $\mu\text{m}$  (b). Most of the data lie within 1 standard deviation of the mean, indicating that the error bars on each measurement are accurate and that the measurements from each foil and aperture are in agreement.

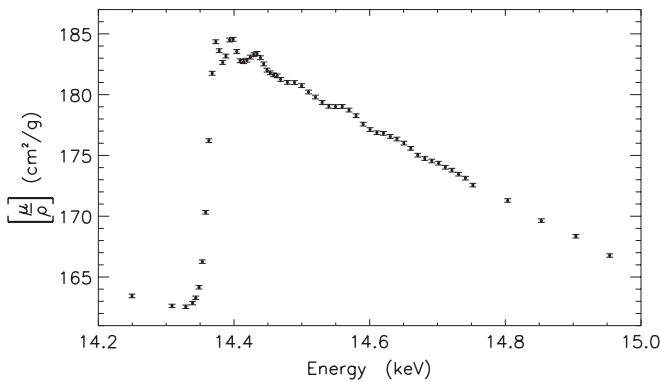


**Figure 10.** The mass-attenuation coefficient is plotted (with experimental error bars) against x-ray energy between 14.2 keV and 15 keV. The gold  $L_I$  absorption edge can be seen at 14.35 keV and the associated XAFS between 14.35 keV and 14.75 keV.

The photoelectric absorption of a material can be expressed in terms of the imaginary part of the form factor  $f''$ :

$$f'' = \frac{m_a}{2hcr_e} \left[ \frac{\mu}{\rho} \right]_{pe}, \quad (16)$$

where  $\left[ \frac{\mu}{\rho} \right]_{pe}$  is the photoelectric mass-absorption coefficient,  $m_a$  is the atomic mass,  $r_e$  is the classical electron radius,  $h$  is Planck's constant and  $c$  is the speed of light [43]. The photoelectric mass-absorption coefficient was calculated by subtracting the contribution from Rayleigh and Compton scattering. The scattering attenuation coefficient was calculated from the average of the FFAST [9] and XCOM [10] tabulations and the uncertainty was assumed to be the difference between the two tabulations divided by  $\sqrt{2}$ . The uncertainty in the scattering attenuation contributed less than 0.03% to the photoelectric absorption and was not a

major source of error. Our measurements should be a good approximation of the imaginary part of the atomic form factor of gold, except at the edge and in the XAFS region between about 14.3 keV and 15 keV, where solid-state effects are significant.

Table 3 gives the values and uncertainties of the calibrated x-ray energy, mass-attenuation coefficient, photoelectric mass-absorption coefficient and imaginary component of the form factor. Column 4 lists the accuracy of the mass-attenuation coefficient measurement excluding the contribution from the absolute calibration. This quantity is useful for XAFS, since most XAFS researchers use attenuation data on a relative scale. We will refer to this quantity as  $\sigma_{\text{XAFS}}$ . A breakdown of the various contributions to the uncertainty in the energy, mass-attenuation coefficient and imaginary part of the form factor is given in table 4.

## 7. X-ray absorption fine structure

The significant x-ray absorption fine structure (XAFS) was observed in our data in the region above the  $L_I$  edge (see figure 10). This structure results from the interaction between the ejected photoelectron and the ordered local structure surrounding the absorbing atoms. The XAFS can be analysed to yield structural information such as bond lengths [44]. For high-Z elements, XAFS measurements are often made at L edges, since they fall within an energy range that is accessible at most synchrotrons. The  $L_{II}$  and  $L_{III}$  edges are often used to study magnetic effects in materials such as magnetic oxides [45], 3D elements [46] and ferromagnetic materials [47].

In gold, XAFS has been used to investigate materials that are inaccessible to techniques such as crystallography. The local structure of gold nanoparticles (clusters, colloids and nanowires) was determined by analysis of the  $L_{II}$  and  $L_{III}$  edge XAFS [48]. The nearest neighbour bond lengths of gold have been determined before at an L edge using XAFS and were found to be 2.877 Å and 4.065 Å (at a temperature of 77 K) [49].

We performed an XAFS analysis on our data and determined bond lengths using a method similar to that of [50]. The measurements were made at a temperature of approximately 293 K. A face centred cubic structure was assumed with the nearest-neighbour bond length as the main fitting parameter. All the other bond lengths were scaled by the same fraction so that the fitting parameter controlled the scale of the structure. As is conventional in the XAFS literature, we use the phrase *bond length* to mean the average interatomic distance [51].

The XAFS analysis and fitting was performed using a modified version of the IFEFFIT computational package [52] which is built upon the FEFF XAFS-simulation code [53]. The IFEFFIT code was modified in a similar manner to [50] so that it correctly interpreted experimental error bars and calculated  $\chi_r^2$  using the conventional definition. The fit was performed by minimizing  $\chi_r^2$  and so the derived parameters and their uncertainties also reflect the conventional  $\chi_r^2$ . In the previous work, the use of this conventional definition of  $\chi_r^2$  has highlighted the poor agreement between theory and

**Table 3.** The mass-attenuation coefficients of gold are tabulated at 91 energies between 14 keV and 21 keV. In columns 1 and 2, the x-ray energy and mass-attenuation coefficient are listed along with the 1 standard deviation uncertainty in the least significant digit(s), which is given in brackets. The percentage uncertainty in the mass-attenuation coefficient is listed in column 3. Column 4 gives the precision of the mass-attenuation coefficient measurements (the uncertainty excluding the contribution from full-foil mapping) which is useful for XAFS researchers. Columns 5 and 6 list the photoelectric mass-absorption coefficient and the imaginary component of the form factor of gold respectively, along with their uncertainties in brackets. The values of  $f''$  between 14.35 keV and 14.8 keV (at and above the edge) include solid-state effects.

Energy (keV)	$[\frac{\mu}{\rho}]$ ( $\text{cm}^2 \text{g}^{-1}$ )	$\frac{\sigma_{[\mu/\rho]}}{[\mu/\rho]}$ (%)	$\sigma_{\text{XAFS}}$ ( $\text{cm}^2 \text{g}^{-1}$ )	$[\frac{\mu}{\rho}]_{pe}$ ( $\text{cm}^2 \text{g}^{-1}$ )	$f''$ (e/atom)
14.2496(6)	163.45(15)	0.09	0.06	160.01(15)	10.672(10)
14.3087(6)	162.62(14)	0.08	0.03	159.20(14)	10.662(9)
14.3289(4)	162.55(14)	0.08	0.03	159.13(14)	10.673(9)
14.3389(4)	162.85(14)	0.08	0.02	159.44(14)	10.701(9)
14.3436(3)	163.29(14)	0.08	0.03	159.87(14)	10.734(9)
14.3484(3)	164.15(14)	0.08	0.03	160.74(14)	10.795(10)
14.3533(3)	166.27(14)	0.08	0.04	162.85(14)	10.941(10)
14.3581(3)	170.32(15)	0.08	0.04	166.91(15)	11.217(10)
14.3628(3)	176.21(16)	0.08	0.06	172.80(16)	11.617(11)
14.3679(3)	181.76(16)	0.08	0.05	178.35(16)	11.994(11)
14.3731(3)	184.35(16)	0.08	0.04	180.94(16)	12.173(11)
14.3781(3)	183.62(16)	0.08	0.04	180.21(16)	12.128(11)
14.3832(3)	182.65(16)	0.08	0.04	179.24(16)	12.067(11)
14.3881(3)	183.18(16)	0.08	0.04	179.77(16)	12.107(11)
14.3935(3)	184.50(16)	0.08	0.04	181.09(16)	12.201(11)
14.3987(3)	184.55(16)	0.08	0.04	181.15(16)	12.209(11)
14.4040(3)	183.55(16)	0.08	0.04	180.15(16)	12.146(11)
14.4091(3)	182.79(16)	0.08	0.04	179.39(16)	12.099(11)
14.4141(3)	182.71(16)	0.08	0.04	179.32(16)	12.098(11)
14.4190(3)	182.84(16)	0.08	0.04	179.44(16)	12.111(11)
14.4241(3)	183.09(16)	0.08	0.04	179.69(16)	12.132(11)
14.4292(3)	183.28(16)	0.08	0.04	179.89(16)	12.150(11)
14.4339(3)	183.39(16)	0.08	0.04	180.00(16)	12.161(11)
14.4390(3)	183.04(16)	0.08	0.04	179.64(16)	12.141(11)
14.4437(3)	182.53(16)	0.08	0.04	179.14(16)	12.111(11)
14.4487(3)	182.01(16)	0.08	0.04	178.62(16)	12.080(11)
14.4534(3)	181.80(16)	0.08	0.04	178.41(16)	12.070(11)
14.4583(3)	181.63(16)	0.08	0.04	178.24(16)	12.063(11)
14.4636(3)	181.55(16)	0.08	0.04	178.16(16)	12.062(11)
14.4687(3)	181.25(16)	0.08	0.04	177.87(16)	12.046(11)
14.4788(4)	181.01(16)	0.08	0.04	177.63(16)	12.038(11)
14.4892(4)	181.00(16)	0.08	0.04	177.62(16)	12.046(11)
14.4997(4)	180.74(16)	0.08	0.04	177.36(16)	12.037(11)
14.5098(4)	180.22(16)	0.08	0.04	176.84(16)	12.011(11)
14.5201(4)	179.80(16)	0.08	0.04	176.43(16)	11.991(11)
14.5300(4)	179.35(16)	0.08	0.04	175.99(16)	11.969(11)
14.5398(4)	179.04(15)	0.08	0.04	175.68(16)	11.956(11)
14.5496(4)	179.02(15)	0.08	0.04	175.65(15)	11.962(11)
14.5596(4)	179.03(15)	0.08	0.04	175.67(15)	11.972(11)
14.5696(4)	178.73(15)	0.08	0.04	175.37(15)	11.960(11)
14.5799(4)	178.27(15)	0.08	0.04	174.91(15)	11.937(11)
14.5903(4)	177.57(15)	0.08	0.04	174.22(15)	11.898(11)
14.6006(4)	177.13(15)	0.08	0.04	173.78(15)	11.876(10)
14.6106(4)	176.87(15)	0.08	0.04	173.52(15)	11.867(10)
14.6203(4)	176.82(15)	0.08	0.04	173.47(15)	11.871(10)
14.6304(4)	176.56(15)	0.08	0.04	173.22(15)	11.862(10)
14.6401(4)	176.35(15)	0.08	0.04	173.01(15)	11.856(10)
14.6504(4)	176.01(15)	0.08	0.04	172.67(15)	11.841(10)
14.6606(4)	175.58(15)	0.08	0.04	172.25(15)	11.820(10)
14.6709(4)	175.02(15)	0.08	0.04	171.69(15)	11.790(10)
14.6812(4)	174.74(15)	0.08	0.04	171.42(15)	11.779(10)
14.6916(4)	174.54(15)	0.08	0.04	171.22(15)	11.774(10)
14.7016(4)	174.36(15)	0.08	0.04	171.04(15)	11.770(10)
14.7116(4)	174.02(15)	0.08	0.04	170.70(15)	11.755(10)
14.7212(4)	173.79(15)	0.08	0.04	170.47(15)	11.746(10)
14.7311(4)	173.46(15)	0.08	0.04	170.14(15)	11.732(10)
14.7411(4)	173.13(15)	0.08	0.04	169.81(15)	11.717(10)
14.7521(4)	172.56(15)	0.08	0.02	169.25(15)	11.687(10)
14.8034(6)	171.29(15)	0.08	0.02	167.99(15)	11.640(10)

**Table 3.** (Continued.)

Energy (keV)	$[\frac{\mu}{\rho}]$ (cm <sup>2</sup> g <sup>-1</sup> )	$\frac{\sigma_{[\mu/\rho]}}{[\mu/\rho]}$ (%)	$\sigma_{\text{XAFS}}$ (cm <sup>2</sup> g <sup>-1</sup> )	$[\frac{\mu}{\rho}]_{pe}$ (cm <sup>2</sup> g <sup>-1</sup> )	$f''$ (e/atom)
14.8531(6)	169.64(14)	0.08	0.02	166.35(14)	11.565(10)
14.9040(6)	168.35(14)	0.08	0.02	165.08(14)	11.516(10)
14.9538(6)	166.77(14)	0.08	0.02	163.51(14)	11.445(10)
15.0046(6)	165.42(14)	0.08	0.02	162.18(14)	11.390(10)
15.0559(6)	163.89(14)	0.08	0.02	160.65(14)	11.321(10)
15.2573(12)	158.54(13)	0.08	0.02	155.35(13)	11.094(10)
15.4578(12)	153.30(13)	0.08	0.02	150.16(13)	10.864(9)
15.6583(12)	148.38(13)	0.08	0.02	145.27(13)	10.647(9)
15.8599(12)	143.58(12)	0.08	0.02	140.52(12)	10.431(9)
16.0616(12)	139.04(12)	0.08	0.01	136.02(12)	10.226(9)
16.2631(12)	134.71(12)	0.08	0.03	131.73(12)	10.028(9)
16.4639(12)	130.53(11)	0.08	0.03	127.60(11)	9.833(9)
16.6652(12)	126.59(11)	0.08	0.03	123.70(11)	9.649(9)
16.8676(12)	122.72(11)	0.08	0.03	119.87(11)	9.464(8)
17.0688(12)	119.10(10)	0.08	0.03	116.28(10)	9.290(8)
17.2708(12)	115.53(10)	0.08	0.03	112.75(10)	9.115(8)
17.4720(12)	112.19(10)	0.08	0.03	109.45(10)	8.951(8)
17.6730(12)	108.92(10)	0.08	0.02	106.21(10)	8.786(8)
17.8735(13)	105.83(9)	0.08	0.02	103.16(9)	8.631(8)
18.0754(13)	102.83(9)	0.08	0.01	100.19(9)	8.477(7)
18.2752(13)	99.95(9)	0.08	0.02	97.35(9)	8.328(7)
18.4766(13)	97.18(8)	0.08	0.02	94.61(8)	8.182(7)
18.6781(13)	94.51(8)	0.08	0.02	91.97(8)	8.041(7)
18.8782(13)	91.94(8)	0.08	0.02	89.44(8)	7.903(7)
19.0795(13)	89.45(8)	0.08	0.01	86.98(8)	7.768(7)
19.2818(13)	87.05(7)	0.08	0.01	84.61(8)	7.636(7)
19.4833(13)	84.76(7)	0.08	0.01	82.35(7)	7.510(7)
19.6832(13)	82.55(7)	0.08	0.01	80.18(7)	7.387(7)
19.8848(15)	80.37(7)	0.08	0.01	78.03(7)	7.263(7)
20.0881(13)	78.34(7)	0.08	0.02	76.03(7)	7.149(7)
20.5894(6)	73.47(6)	0.08	0.01	71.21(6)	6.863(6)
21.0919(6)	69.02(6)	0.08	0.02	66.79(6)	6.594(6)

**Table 4.** A breakdown of the contributions to the uncertainty in the mass-attenuation coefficient, imaginary component of the form factor and the x-ray energy. The uncertainty due to impurities, roughness and energy drift only had an appreciable effect for some measurements. The final results were produced from a weighted mean and are much less affected by these systematic errors than this table suggests.

Quantity	Uncertainty	Comment
$[\frac{\mu}{\rho}]$	0.083%	Accuracy of the full-foil mapping
	<0.06%	Impurities in the 99.9% foils
	<0.06%	Roughness of the 5 $\mu\text{m}$ foil
	<0.03%	Uncertainty due to the energy drift
$f''$	0.08–0.1%	Contribution from $[\frac{\mu}{\rho}]$ uncertainty
	<0.03%	Scattering contribution uncertainty, largest just below the $L_I$ edge
Energy	0.3 eV–1.3 eV	Accuracy limited by powder-diffraction results
	<0.1 eV	Uncertainty due to the energy drift

experiment. Despite using a fairly narrow window,  $\chi_r^2$  was always between 60 and 180 [50].

The edge-energy estimate  $E_0$  was taken to be the point of maximum derivative of the attenuation coefficient and was found to be 14362.81 eV. The fit was performed in  $k$  space between  $k = 2.7 \text{ \AA}^{-1}$  and  $16 \text{ \AA}^{-1}$  and was not  $k$ -

weighted. Since the fitting was done in  $k$  space, no Fourier transforms were performed and therefore no window tapering was required. The local structure of the gold was modelled using FEFF (version 8.1) [53] using 20 paths (the addition of more paths did not improve agreement with experiment). The background spline was not refined during the fit.

The quality of the fit was excellent (figure 11) and  $\chi_r^2$  was 1.94. The nearest-neighbour bond length was found to be  $2.879 \pm 0.004 \text{ \AA}$ . The second-nearest-neighbour bond length was determined to be  $4.076 \pm 0.006 \text{ \AA}$ , the  $\Delta E_0$  parameter was fitted to be  $3.2 \pm 0.3 \text{ eV}$  and the Debye temperature  $\theta_D$  was fitted to be  $232^\circ \pm 14^\circ$ . The many-body amplitude reduction factor  $S_0^2$  was found to be  $0.76 \pm 0.03$ . The value of conventional  $\chi_r^2$  achieved here is much better than the previous work, despite having experimental error bars of a similar magnitude and a wider window.

It is interesting to compare the structure determined by our XAFS analysis with those from crystallography. The value we determined for the second nearest-neighbour bond length can be compared to the crystallographic lattice parameter. These quantities are two different ways of measuring the distance between two atoms. The XAFS bond length corresponds to the average distance between the two atoms and crystallographic length measures the distance between the mean positions of the atoms or lattice positions [54]. For a close-packed, high-Z, symmetric system such as fcc gold, the difference between

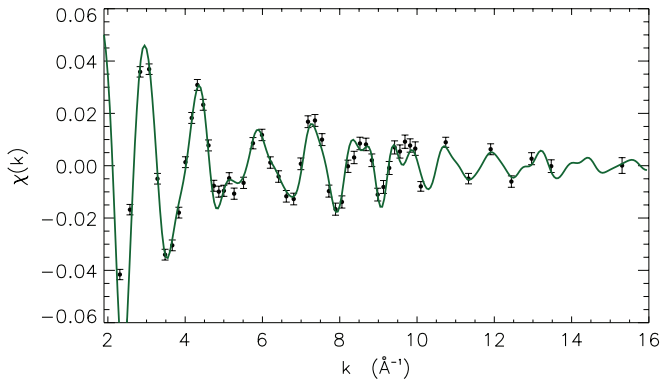


**Figure 11.** The plot compares the experimental and fitted structures of the gold XAFS above the  $L_I$  edge. The standard XAFS signal  $\chi(k)$  is plotted and should not be confused with the goodness-of-fit parameter  $\chi_r^2$ . The experimental measurements are plotted in black along with error bars reflecting their experimental uncertainties. The FEFF prediction is plotted as a dark green line and is based on the best-fit parameters. The agreement between the two is excellent ( $\chi_r^2 = 1.94$ ).

the two measures is small compared with the accuracy of this measurement. Wyckoff measured the lattice parameter to be 4.078 Å at 291 K [55]. Suh *et al* measured the lattice parameter of gold at 293 K to be 4.072 Å [56]. Both of these crystallographic measurements are in good agreement with our XAFS determination (within 1 standard deviation). The excellent agreement between our structural determination and those from crystallography helps confirm the quality of the experimental data and the fit.

## 8. Comparison with other measurements and theory

### 8.1. Comparison with previous experimental results

There have been several previous measurements of the mass-attenuation coefficient of gold in this energy range. Table 1 summarizes the details of the eight publications that included estimates of their uncertainties (25 measurements in total). These earlier measurements had uncertainties ranging from 1% to 3%, except for a single point measurement at 14.4 keV by Alonso and Grodzins [18] which claimed an accuracy of 0.1% and three measurements by Hughes *et al* [17] who claimed an accuracy of 0.5%.

In figure 12, our results are compared with these earlier measurements. Given our quoted uncertainty, our data are in reasonable agreement with the results of Parthasaradhi, Laubert, Rao and Del Grande and generally lie within 1.5 standard deviations. Our results are discrepant from the measurements of Bearden and Hanser by twice their estimated experimental uncertainty. The results of Allen are higher than our measurements by around 12% which is 12 times the experimental uncertainty—however, it is a very early measurement, having been made in 1924.

The most interesting comparison is with the most accurate measurements. Alonso and Grodzins [18] claimed to have measured the mass-attenuation coefficient of gold at 14.4 keV to an accuracy of 0.1%—a claim five times more accurate

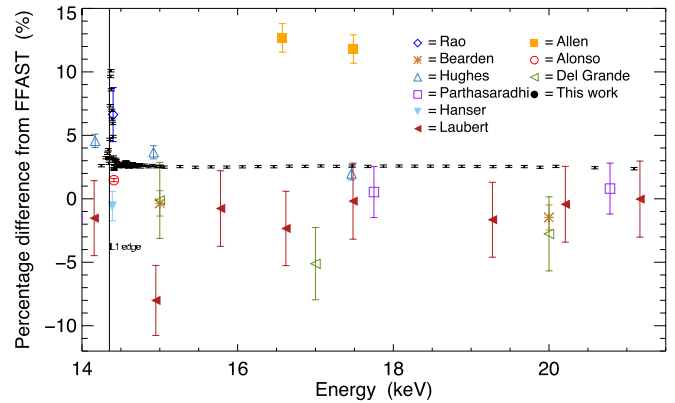


**Figure 12.** The plot compares our measurements of the mass-attenuation coefficient of gold with the results of previous experiments by plotting  $100 \frac{\text{EXP} - \text{FFAST}}{\text{FFAST}}$ . All the measurements have error bars, which indicate the authors' quoted experimental uncertainty (see table 1 for references). The solid vertical line marks the energy of the gold  $L_I$  edge.

than any measurement before ours. However, the energy of the x-ray beam was only specified to one decimal place (in keV). They used multiple foil thicknesses and also corrected for some systematic effects such as impurities and scattering. The integrated column density was determined by dividing the mass of the foil by its area, but no full-foil map was performed. They therefore assumed the entire foil to be of uniform thickness. Metal foils typically show a thickness variation of a few per cent (the gold foils used in this experiment varied over a range of about 4% during the raster scan), and the previous work has shown that this causes a systematic reduction in the measured mass-attenuation coefficient [57]. It is therefore not surprising that our measurement at 14.4 keV differs from that of Alonso and Grodzins by 0.85% (or eight times their quoted uncertainty).

The next most accurate measurement of the mass-attenuation coefficient of gold in this energy range is that of Hughes *et al* [17] who claimed an accuracy of 0.5%. Of the three measurements in this energy range, two are in good agreement with our measurements. The third measurement (at 14 170 eV) appears to be about 3 standard deviations higher.

### 8.2. Comparison with theory

We compared our results with the most commonly used theoretical tabulations (FFAST and XCOM) in figure 13. Across almost the entire energy range, our experimental results are about 2.5% greater than the corresponding values of the FFAST tabulation. The XCOM tabulation is in better agreement with our results with a discrepancy in the 0.5–1.5% range. The scatter of the experimental points between 14.3 keV and 15 keV is the x-ray absorption fine structure (XAFS) due to solid-state effects.

The consistency of the magnitude of the discrepancy between our experiment and FFAST is quite unexpected. In several XERT experiments at K-edges the discrepancy was largest just above the edge and decreased at higher energies. The discrepancy between experiment and FFAST at K-edges

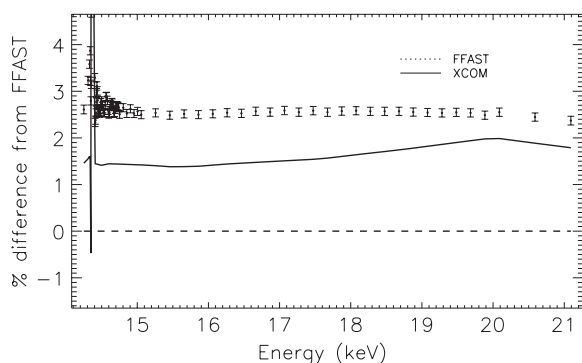


**Figure 13.** Our measurements of the mass-attenuation coefficient of gold are compared with the theoretical predictions of the FFAST and XCOM tabulations. The experimental measurements are significantly larger than both theoretical tabulations over the entire energy range. XCOM is in better agreement with these measurements.

has been repeatedly observed [12–15, 28, 33] but remains unexplained. The absence of energy dependence in the discrepancy at the gold  $L_I$  edge is interesting and yet more unexpected, and raises several questions.

- Does gold exhibit an energy-dependent discrepancy at the K-edge?
- Why does the energy-dependent effect seem to appear at K-edges but not at the gold  $L_I$  edge?
- What is the cause of the near-constant discrepancy between FFAST and this experiment?
- What is the nature of the discrepancy at the gold  $L_I$  and  $L_{II}$  edges or at the L edges of other elements?

The cause of the observed discrepancies is yet to be established. The resolution of these questions may not come until new and more accurate theoretical tabulations are produced in the years ahead.

## 9. Conclusion

The x-ray mass-attenuation coefficients of gold were measured at 91 energies between 14 keV and 21 keV. The measurements were accurate to between 0.08% and 0.1% after the removal of a number of systematic errors that affected our measurements. The photoelectric mass-absorption coefficient and the imaginary component of the form factor were also determined for the same x-ray energies.

An XAFS analysis was performed that yielded accurate values of bond lengths of gold. The analysis showed that with accurate experimental data and correct propagation of experimental uncertainties, excellent agreement between XAFS from experiment and theory can be obtained (as reflected in the value of  $\chi_r^2$ ).

The results were compared with earlier measurements and revealed deficiencies in many of these. A comparison was also made with the major theoretical tabulations, exposing some inadequacies and raising several questions about the theoretical calculation of attenuation coefficients at L edges. The observed discrepancies suggest that more work is required to produce accurate tabulations of mass-attenuation coefficients and form factors.

## Acknowledgments

We wish to acknowledge the assistance of the beamline staff, David Cookson and Garry Foran, during the experiment at the Photon Factory (ANBF). We wish to acknowledge the developmental work of Martin D de Jonge on XERT analysis techniques including the full-foil mapping technique. This work was supported by the Australian Synchrotron Research Program, which is funded by the Commonwealth of Australia under the Major National Research Facilities Program, and by grants of the Australian Research Council.

## References

- [1] Röntgen W C 1895 Ueber eine neue Art von Strahlen: vorläufige Mitteilung *Sitzungsberichte Med. Phys. Ges. Würzburg* **137** 132–41
- [2] Lee M J, Hahn P F, Papanicolaou N, Egglin T K, Saini P R, Mueller S and Simeone J F 1991 Benign and malignant adrenal masses: CT distinction with attenuation coefficients, size, and observer analysis *Radiology* **179** 415–8
- [3] Terwilliger T C and Berendzen J 1999 Automated MAD and MIR structure solution *Acta Crystallogr.* **55** 849–61
- [4] Hendrickson W A, Horton J R and LeMaster D M 1990 Selenomethionyl proteins produced for analysis by multiwavelength anomalous diffraction (MAD): a vehicle for direct determination of three-dimensional structure *EMBO J* **9** 1665–72
- [5] Han S W, Stern E A, Haskel D and Moodenbaugh A R 2002 Local structure in the stripe phase of  $\text{La}_{1.6-x}\text{Sr}_x\text{Nd}_{0.4}\text{CuO}_4$  *Phys. Rev. B* **66** 094101
- [6] Ignatov A Yu, Ali N and Khalid S 2001 Mn K-edge XANES study of the  $\text{La}_{1-x}\text{Ca}_x\text{MnO}_3$  colossal magnetoresistive manganites *Phys. Rev. B* **64** 014413
- [7] Creagh D C and Hubbell J H 1987 Problems associated with the measurement of X-ray attenuation coefficients: I. Silicon. Report of the International Union of Crystallography X-ray Attenuation Project *Acta. Cryst. A* **43** 102–12
- [8] Tran C Q, Chantler C T and Barnea Z 2003 X-ray mass attenuation coefficient of silicon: theory versus experiment *Phys. Rev. Lett.* **90** 257401
- [9] Chantler C T 2000 Theoretical form factor, attenuation, and scattering tabulation for  $Z = 1-92$  from  $E = 1-10$  eV to  $E = 0.4-1.0$  MeV *J. Phys. Chem. Ref. Data* **29** 597
- [10] Berger M J, Hubbell J H, Seltzer S M, Coursey J S and Zucker D S 1998 XCOM: photon cross sections database *Database* **1** 1
- [11] Chantler C T, Olsen K, Dragoset R A, Chang J, Kishore A R, Kotochigova S A and Zucker D S 2005 X-Ray Form factor, attenuation and scattering tables (version 2.1) *Technical Report* National Institute of Standards and Technology, Gaithersburg, MD (also available at '<http://physics.nist.gov/ffast>')
- [12] Kodre A, Padežnik Gomilšek J, Mihelič A and Arčon I 2006 X-ray absorption in atomic Cd in the K-edge region *Radiat. Phys. Chem.* **75** 188–94
- [13] Tran C Q, Chantler C T, Barnea Z, de Jonge M D, Dhal B B, Chung C T Y, Paterson D and Wang J 2005 Measurement of the x-ray mass attenuation coefficient of silver using the x-ray-extended range technique *J. Phys. B At. Mol. Phys.* **38** 89–107
- [14] Chantler C T, Tran C Q, Barnea Z, Paterson D, Cookson D J and Balaic D X 2001 Measurement of the x-ray mass attenuation coefficient of copper using 8.85–20 keV synchrotron radiation. *Phys. Rev. A* **64** 062506

- [15] de Jonge M D *et al* 2007 Measurement of the x-ray mass attenuation coefficient and determination of the imaginary component of the atomic form-factor of tin over the energy range of 29 keV–60 keV *Phys. Rev. A* **75** 032702
- [16] Islam M T, Rae N A, Glover J L, Barnea Z, de Jonge M D, Tran C Q, Wang J and Chantler C T 2010 Measurement of the x-ray mass attenuation coefficients of gold in the 35 keV–50 keV energy range *Phys. Rev. A* **81** 022903
- [17] Hughes G D, Woodhouse J B and Bucklow I A 1968 The determination of some x-ray mass absorption coefficients *Br. J. Appl. Phys.* **1** 695
- [18] Alonso J and Grodzins L 1965 Measurement of total attenuation cross sections in aluminum and gold for 14.4-keV gamma rays *Phys. Rev.* **137** 975–8
- [19] Hubbell J H 1995 Bibliography of photon total cross section (attenuation coefficient) measurements *Technical Report Ionizing Radiation Division, National Institute of Standards and Technology, Gaithersburg, MD, USA* (<http://physics.nist.gov/PhysRefData/photons/html/attencoef.html>)
- [20] Allen S J M 1926 The absorption of X-rays from  $\lambda = .08$  to 4.0 Å *Phys. Rev.* **28** 907–22
- [21] Laubert S 1941 Die Massenschwächungs-, Photoabsorptions- und Streukoeffizienten monochromatischer Röntgenstrahlen von Ni (28), Cu (29), Ag (47), Cd (48), Sn (50), Ta (73), W (74), Ir (77), Pt (78), Au (79) und Pb (82) *Ann. Phys., Lpz.* **432** 553–78
- [22] Bearden A J 1966 X-ray photoeffect cross sections in low- and medium-*z* absorbers for the energy range 852 eV to 40 keV *J. Appl. Phys.* **37** 1681
- [23] Parthasaradhi K and Hansen H H 1974 Attenuation-coefficient measurements for 3.3- to 165.8-keV photons: analysis in terms of total photoelectric cross sections *Phys. Rev. A* **10** 563–568
- [24] Hanser Frederick A and Sellers Bach 1974 Measurement of totally depleted silicon solid state detector thickness by x-ray attenuation *Rev. Sci. Instrum.* **45** 226–31
- [25] Rao V V and Shahnawaz 1978 Photoelectric cross-sections of low-energy photons *Il Nuovo Cimento A* **44** 181
- [26] Del Grande N K 1986 Measured 1 to 40 keV photoabsorption cross sections for: Fe, Ni, Sn, Ta, Pt, Au, Pb, U *Proc. SPIE* **691** 2–9
- [27] Creagh D C and Hubbell J H 1990 Problems associated with the measurement of X-ray attenuation coefficients: II. Carbon. Report on the international union of crystallography x-ray attenuation project *Acta Cryst. A* **108** 7673
- [28] de Jonge M D, Tran C Q, Chantler C T, Barnea Z, Dhal B B, Cookson D J, Lee W-K and Mashayekhi A 2005 Measurement of the x-ray mass attenuation coefficient and determination of the imaginary component of the atomic form factor of molybdenum over the 13.5–41.5-keV energy range *Phys. Rev. A* **71** 032702
- [29] Tran C Q, Barnea Z, Jonge M D de, Dhal B B, Paterson D, Cookson D J and Chantler C T 2003 Quantitative determination of major systematics in synchrotron x-ray experiments: seeing through harmonic components *X-Ray Spectrom.* **32** 69–74
- [30] de Jonge M D, Barnea Z, Tran C Q and Chantler C T 2004 X-ray bandwidth: Determination by on-edge absorption and effect on various absorption experiments *Phys. Rev. A* **69** 022717
- [31] Tran C Q, de Jonge M D, Barnea Z and Chantler C T 2004 Absolute determination of the effect of scattering and fluorescence on x-ray attenuation measurements *J. Phys. B: At. Mol. Opt. Phys.* **37** 3163–76
- [32] Glover J L, Chantler C T and de Jonge M D 2009 Nano-roughness in gold revealed from x-ray signature *Phys. Lett. A* **373** 1177–80
- [33] Glover J L, Chantler C T, Barnea Z, Rae N A, Tran C Q, Creagh D C, Paterson D and Dhal B B 2008 Measurements of the x-ray mass-attenuation coefficient and imaginary component of the form factor of copper *Phys. Rev. A* **78** 032702
- [34] de Jonge M D 2005 High accuracy measurements of the x-ray mass attenuation coefficients of molybdenum and tin: testing theories of photoabsorption *PhD Thesis University of Melbourne* (available from <http://eprints.infodiv.unimelb.edu.au/archive/00002201/>)
- [35] Nordfors B 1960 The statistical error in x-ray absorption measurements *Arkiv Fysik* **18** 37
- [36] Wilson A J C and Prince E 1999 *International Tables for Crystallography* vol C (Boston, MA: Kluwer)
- [37] Rasberry S, Hubbard C, Zhang Y and McKenzie R 1989 Standard Reference Material Certificates, Standard Reference Material 660, NIST
- [38] Rae N A, Chantler C T, Tran C Q and Barnea Z 2006 Accurate determination of X-ray energies using powder diffraction *Radiat. Phys. Chem.* **75** 2063–6
- [39] de Jonge M D, Barnea Z, Tran C Q and Chantler C T 2004 Full-foil x-ray mapping of integrated column density applied to the absolute determination of mass attenuation coefficients *Meas. Sci. Technol.* **15** 1811–22
- [40] Barnea Z and Mohyla J 1974 Detection of the contribution of harmonics to the diffracted x-ray intensity *J. Appl. Cryst.* **7** 298–9
- [41] Glover J L and Chantler C T 2009 A method to determine the absolute harmonic content of an X-ray beam using attenuation measurements *X-Ray Spectrom.* **38** 510–12
- [42] Thompson A C and Vaughan D 2001 and Center for X-ray optics and Advanced Light Source *X-Ray Data Booklet* (Lawrence Berkeley National Laboratory, University of California)
- [43] Mohr P J and Taylor B N 2000 CODATA recommended values of the fundamental physical constants: 1998 *Rev. Mod. Phys.* **72** 351–495
- [44] Chen G, Jain H, Khalid S, Li J, Drabold D A and Elliott S R 2001 Study of structural changes in amorphous As<sub>2</sub>Se<sub>3</sub> by EXAFS under *in situ* laser irradiation *Solid State Commun.* **120** 149–53
- [45] Ahlers D, Attenkofer K and Schutz G 1998 Spin-dependent extended x-ray absorption fine structure in magnetic oxides *J. Appl. Phys.* **83** 7085
- [46] Lemke L *et al* 1998 Magnetic extended x-ray absorption fine structure at the L 3.2 edges of 3d elements *J. Phys.: Condens. Matter* **10** 1917–30
- [47] Krishnamurthy V V, Suzuki M, Kawamura N, Ishikawa T and Kohori Y 2002 Iridium L<sub>2,3</sub> edge magnetic circular dichroism study of 5d moment formation in ferromagnetic Ir–Fe alloys *Phys. B: Phys. Condens. Matter* **312** 647–9
- [48] Benfield R E, Grandjean D, Kroll M, Pugin R, Sawitowski T and Schmid G 2001 Structure and bonding of gold metal clusters, colloids, and nanowires studied by EXAFS, XANES, and WAXS *J. Phys. Chem. B* **105** 1961–70
- [49] Li G G, Bridges F and Booth C H 1995 X-ray-absorption fine-structure standards: A comparison of experiment and theory *Phys. Rev. B* **52** 6332–48
- [50] Smale L F, Chantler C T, de Jonge M D, Barnea Z and Tran C Q 2006 *Rad. Phys. Chem.* **75** 1559–63
- [51] Newville M, Fulton J L, Pfund D M, Wallen S L, Stern E A and Ma Y 1997 XAFS measurements of Rb–O bonds in ambient and supercritical water *J. Phys. IV France* **7** C2–1007
- [52] Newville M 2001 *J. Synchrotron Rad.* **8** 322
- [53] Ankudinov A L, Ravel B, Rehr J J and Conradson S D 1998 Real-space multiple-scattering calculation and interpretation of x-ray-absorption near-edge structure *Phys. Rev. B* **58** 7565–76

- [54] Dalba G and Fornasini P 1997 EXAFS Debye–Waller factor and thermal vibrations of crystals *J. Synchrotron Radiat.* **4** 243–55
- [55] Wyckoff R W G 1963 *Crystal Structures* (New York: Wiley)
- [56] Suh I K, Ohta H and Waseda Y 1988 High-temperature thermal expansion of six metallic elements measured by dilatation method and X-ray diffraction *J. Mater. Sci.* **23** 757–60
- [57] Tran C Q, Chantler C T, Barnea Z and de Jonge M D 2004 Accurate determination of the thickness or mass per unit area of thin foils and single-crystal wafers for x-ray attenuation measurements *Rev. Sci. Instrum.* **75** 2943–9